https://ntrs.nasa.gov/search.jsp?R=20180006101 2019-04-29T10:26:27+00:00Z

NASA/TM—2018-219912

Effect of Thin-Film Adhesives on Mode II Interlaminar Fracture Toughness in Carbon Fiber Composites With Shape Memory Alloy Inserts

Derek J. Quade
Glenn Research Center, Cleveland, Ohio

Sadhan C. Jana, Gregory N. Morscher, and Manigandan Kanaan
The University of Akron, Akron, Ohio

Linda McCorkle
Ohio Aerospace Institute, Brook Park, Ohio

August 2018

NASA STI Program . . . in Profile

Since its founding, NASA has been dedicated to the advancement of aeronautics and space science. The NASA Scientific and Technical Information (STI) Program plays a key part in helping NASA maintain this important role.

The NASA STI Program operates under the auspices of the Agency Chief Information Officer. It collects, organizes, provides for archiving, and disseminates NASA's STI. The NASA STI Program provides access to the NASA Technical Report Server—Registered (NTRS Reg) and NASA Technical Report Server—Public (NTRS) thus providing one of the largest collections of aeronautical and space science STI in the world. Results are published in both non-NASA channels and by NASA in the NASA STI Report Series, which includes the following report types:

- TECHNICAL PUBLICATION. Reports of completed research or a major significant phase of research that present the results of NASA programs and include extensive data or theoretical analysis. Includes compilations of significant scientific and technical data and information deemed to be of continuing reference value. NASA counter-part of peer-reviewed formal professional papers, but has less stringent limitations on manuscript length and extent of graphic presentations.

- TECHNICAL MEMORANDUM. Scientific and technical findings that are preliminary or of specialized interest, e.g., "quick-release" reports, working papers, and bibliographies that contain minimal annotation. Does not contain extensive analysis.

- CONTRACTOR REPORT. Scientific and technical findings by NASA-sponsored contractors and grantees.

- CONFERENCE PUBLICATION. Collected papers from scientific and technical conferences, symposia, seminars, or other meetings sponsored or co-sponsored by NASA.

- SPECIAL PUBLICATION. Scientific, technical, or historical information from NASA programs, projects, and missions, often concerned with subjects having substantial public interest.

- TECHNICAL TRANSLATION. English-language translations of foreign scientific and technical material pertinent to NASA's mission.

For more information about the NASA STI program, see the following:

- Access the NASA STI program home page at http://www.sti.nasa.gov

- E-mail your question to help@sti.nasa.gov

- Fax your question to the NASA STI Information Desk at 757-864-6500

- Telephone the NASA STI Information Desk at 757-864-9658

- Write to:
  NASA STI Program
  Mail Stop 148
  NASA Langley Research Center
  Hampton, VA 23681-2199

NASA/TM—2018-219912

Effect of Thin-Film Adhesives on Mode II Interlaminar Fracture Toughness in Carbon Fiber Composites With Shape Memory Alloy Inserts

Derek J. Quade
Glenn Research Center, Cleveland, Ohio

Sadhan C. Jana, Gregory N. Morscher, and Manigandan Kanaan
The University of Akron, Akron, Ohio

Linda McCorkle
Ohio Aerospace Institute, Brook Park, Ohio

National Aeronautics and
Space Administration

Glenn Research Center
Cleveland, Ohio 44135

August 2018

This report is a formal draft or working paper, intended to solicit comments and ideas from a technical peer group.

This work was sponsored by the Advanced Air Vehicle Program at the NASA Glenn Research Center

Trade names and trademarks are used in this report for identification only. Their usage does not constitute an official endorsement, either expressed or implied, by the National Aeronautics and Space Administration.

Level of Review: This material has been technically reviewed by technical management.

Available from

NASA STI Program
Mail Stop 148
NASA Langley Research Center
Hampton, VA 23681-2199

National Technical Information Service
5285 Port Royal Road
Springfield, VA 22161
703-605-6000

This report is available in electronic form at http://www.sti.nasa.gov/ and http://ntrs.nasa.gov/

Effect of Thin-Film Adhesives on Mode II Interlaminar Fracture Toughness in Carbon Fiber Composites With Shape Memory Alloy Inserts

Derek J. Quade
National Aeronautics and Space Administration
Glenn Research Center
Cleveland, Ohio 44135

Sadhan C. Jana, Gregory N. Morscher, and Manigandan Kanaan
The University of Akron
Akron, Ohio 44325

Linda McCorkle
Ohio Aerospace Institute
Brook Park, Ohio 44142

Summary

A single sheet of NiTi shape memory alloy (SMA) was introduced within a HexPly® 8552/IM7 (Hexcel®) polymer matrix composite (PMC) panel in conjunction with multiple thin-film adhesives to promote the interfacial bond strength between the SMA and PMC. End-notched flexure (ENF) testing was performed in accordance with the ASTM D7905 method for evaluation of mode II interlaminar fracture toughness (G_{IIC}) of unidirectional fiber-reinforced PMCs. Acoustic emissions (AEs) were monitored during testing with two acoustic sensors attached to the specimens. The composite panels were subjected to a C-scan before testing and examined using optical and scanning electron microscopy (SEM) techniques after part failure. G_{IIC} values for the control composite samples were found to be higher than those of samples with embedded SMA sheets. The presence of adhesives bonded to SMA sheets further diminished the G_{IIC} values. AE values revealed poor bonding of the panels, with little to no signals during testing.

1.0 Introduction

The fabrication and testing of hybrid materials of shape memory alloys (SMAs) and polymer matrix composites (PMCs) have been a growing area of research interest in the past decade. Such research studies include debonding of NiTi wires from composites of carbon fiber (Ref. 1) and epoxy systems (Refs. 2 to 4) and NiTi strips embedded in specimens for thermomechanical testing (Refs. 4 and 5). SMA inclusion into chevrons (Ref. 6) as well as systems designed to test their response from bending (Ref. 7) and buckling (Ref. 8) within composites has been reported. Modeling of SMAs within composite systems has been attempted (Refs. 9 and 10). The SMAs ability to induce large amounts of stress from heating while embedded within polymers has opened a new area of interest on hybrid actuators (Refs. 11 to 13). In order to advance this technology properly, further testing is required to fully understand and optimize the bonds between these dissimilar materials.

The root of this type of actuator depends on the physical properties of the SMA itself. The SMA is able to generate large amounts of stress when constricted through reversible, thermoelastic martensitic

transitions of the crystalline structures (Ref. 14). Austenitic crystals shift to a variety of martensitic structures during times of loading or heating. This shift is directly responsible for the aforementioned stresses generated when constricted, as is the case when embedded within a composite (Ref. 15). The bending and flex that occur within an SMA–PMC actuator system depend highly on the interlaminar strength between the individual materials.

Prior investigations involving SMA inclusion within composites focused on the modeling of the actuator stresses (Refs. 6 and 11), enhancing the bond between metal and polymer (Refs. 1 to 4 and 10), or construction of a NiTi-based actuator system (Refs. 6 to 8 and 10 and 12). The majority of these studies utilize optically clear materials (Refs. 2 to 12) that comprise glass and aramid fibers and optically clear resins. Within these systems, stresses and debonding can be monitored with optical methods, such as Raman spectroscopy. Limited studies investigate the interactions between SMAs and PMCs that are not optically clear, typically involving carbon fiber reinforced polymer (CFRP) (Refs. 1, 16, and 17).

The goal of this research was to assess the effects of thin-film adhesives on the interlaminar strength between an SMA and PMC in an actuator. A series of 22-ply unidirectional composite panels were fabricated. Two of the three SMA panels included additional thin-film adhesive between the SMA and PMC in order to optimize bonding. Modified three-point bend testing was performed in accordance with ASTM D7905 standard (Ref. 18). During testing, two acoustic sensors were attached to the specimens to monitor acoustic emissions (AEs). AE was used in order to provide a method of detecting debonding within specimens during interlaminar failure, a process that is usually monitored in prior research using visual methods.

2.0 Experimental Techniques

2.1 Polymer Matrix Composite (PMC) Panel Layup

PMC panel layup was based on ASTM D7905 Method (Ref. 18). PMC panels of an average thickness of 3.55 mm were fabricated by organizing 22 panels with 0° unidirectional plies. This structure is schematically shown in Figure 1. Of these, 11 plies of material were put on either side of a single sheet of SMA material. A nonstick insert is placed between the SMA and PMC as a precrack in the test specimen. The control materials were fabricated with no SMA or with no adhesives, but contained the precrack per the standard.

2.2 Materials and Fabrication

Flat, annealed NiTi sheets were supplied by Johnson Matthey, measuring 457.2 mm long, 101.6 mm wide, and 0.127 mm thick. The SMA strips were cut into rectangular specimens 152.4 mm long by 101.6 mm wide. The SMA specimens were wiped with acetone and dried before insertion in the PMC. The PMC used was a HexPly® 8552 epoxy matrix embedded with IM7 carbon fibers obtained from Hexcel® (Ref. 19). For control samples, no adhesive was placed between the NiTi section and PMC. The rest of the samples were bonded using Hysol® EA9696 (Henkel Corporation) (Ref. 20) and FM® 377U (Cytec Solvay Group) (Ref. 21) thin-film adhesives. The precrack insert used for these tests was a thin polyimide film, measuring 0.0127 mm thick, 25.4 mm wide, and 55.88 mm long. The insert was coated with a mold release agent and heated to 200 °C for 1 hr in order to prevent the PMC from bonding with the insert.

The composite specimens were assembled into 152.4 by 152.4 mm panels, according to the layup guidelines presented in Figure 1. The panels were processed in an autoclave per the required procedure for the HexPly® 8552/IM7 (Ref. 19) PMC panel. The panels were first cured for 1 hr at 110 °C under full vacuum and a pressure of 0.1 MPa. The temperature was then ramped up to 176 °C and vacuum vented

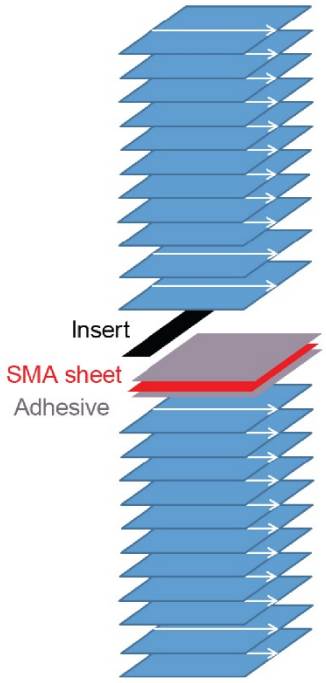

Figure 1.—Panel layup configuration for end-notched flexure testing with 11 plies on each side of shape memory alloy (SMA) sheeting reinforced with thin-film adhesive, nonstick insert included as precrack.

when the pressure increased beyond 0.2 MPa to a total pressure of 0.68 MPa for 2 hr. After curing, each panel was cut into 25.4-mm-wide by 152.4-mm-long specimens for conducting tests. The edges of the specimens were coated in white spray paint to assist in the visual detection of the delamination tip and making compliance calibration (CC) markings. Four marks were placed on the specimens; one to mark the tip of the insert and three placed at distances of 20, 30, and 40 mm from the tip of the insert.

2.3 Mechanical Testing

Tests were conducted on an Instron® 5582 testing device (Instron® Corporation) running the Bluehill® V 2.0 software suite (Instron® Corporation). Two acoustic sensors were attached to the specimens at the end opposite of the crack insert, on opposing sides of the bottom support roller. Vacuum grease was used to maintain contact with the specimen while the clips held the sensors to the specimen. The acoustic sensors were connected to a Digital Wave preamplifier (Digital Wave Corporation), which in turn was connected to a computer running the WaveExplorer software suite (Digital Wave Corporation). The AE sampling rate was 10 MHz, while 2,048 data points for each waveform were recorded, which also included 512 data points per trigger point. Lead break tests were performed on the specimens before the test to make sure the AE sensors were in the correct locations and functioning properly. An end-notched flexure (ENF) setup was used for testing. The ENF test involves loading a sample in three-point bend fixture with a midplane starter crack at the left end, indicated by the distance (a_i). This test setup is shown in Figure 2.

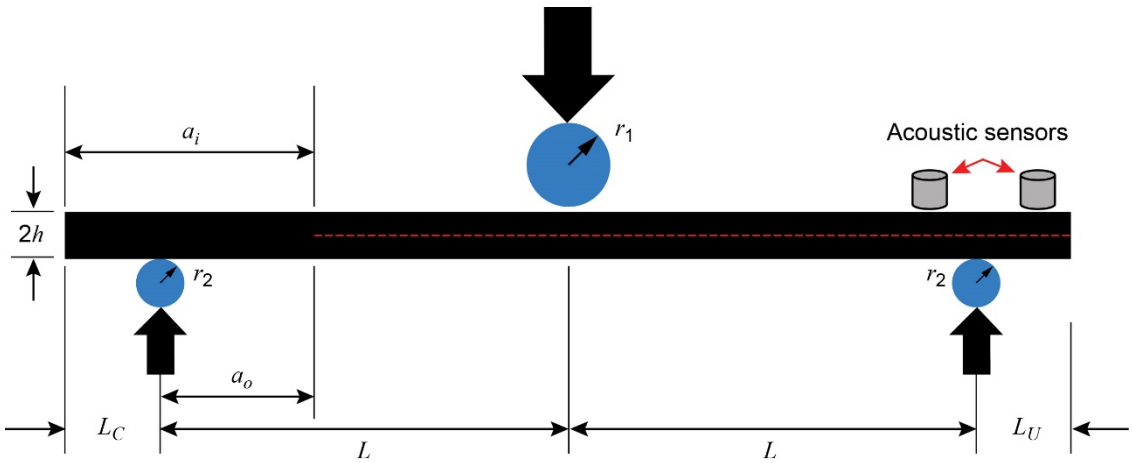

Figure 2.—End-notched flexure three-point bend test. Where a_i is distance, a_o is crack length, h is specimen thickness, L is half-span length, L_C is distance from center of support roller at cracked end of specimen to cracked end of specimen, L_U is distance from center of support roller at uncracked end of specimen to uncracked end of specimen, r_1 is radius of loading roller, and r_2 is radius of support roller.

The crack length (a_o) was initially measured from the support roller with a half-span length, L, spanning the distance from the support rollers to the center loading roller. A CC test was performed in order to find the relationship between specimen compliance and crack length. Three loadings were used to obtain three plots of compliances versus crack length. The first two loadings used a load below failure to prevent delamination. For the first load, the specimen was positioned in the three-point-bend fixture with the left bottom-roller support below the 20-mm mark. A load and unload sequence was applied to acquire compliance for the specimen. This procedure was repeated, shifting the specimen so the bottom support roller would be positioned below the 40-mm and subsequently 30-mm mark. At the 30-mm mark, the specimen was loaded until the crack extended and then the load was removed.

A duo of acoustic sensors was attached to each specimen during testing. As the specimens were tested, acoustic events were recorded and marked at each point they occurred. Before the start of each test, pencil lead breaks (0.5 mm diameter) were performed at the edge of the samples so that the sound traveled across both sensors. The time difference of arrival between the sensors was monitored for the first peak (extensional mode). From these peaks, the speed of sound across the specimens was calculated by the distance between the two sensors (x) divided by the difference in arrival time (Δt_x).

Optical microscopy was performed on an Olympus Microscope DFC295 (Olympus Corporation) utilizing the Leica Applications Suite software (Leica Microsystems), while scanning electron microscopy (SEM) was performed on a Hitachi S-4700 electron microscope (Hitachi High Technologies in America).

3.0 Results

The analysis of data yielded information on fracture toughness. The AE energy signals recorded at the time of experiments were added to load-versus-extension graphs to facilitate data interpretation.

3.1 Mechanical Results

Mechanical tests were performed via the compliance calibration method. For this method, the specimen was flexed in two different locations before crack propagation was progressed at a third location. These three loadings were applied to generate three plots of compliances versus crack length for each specimen. Both the load and unload sequences were recorded within the Bluehill® software suite. The results of this testing are shown below for each specimen in Figure 3 to Figure 6.

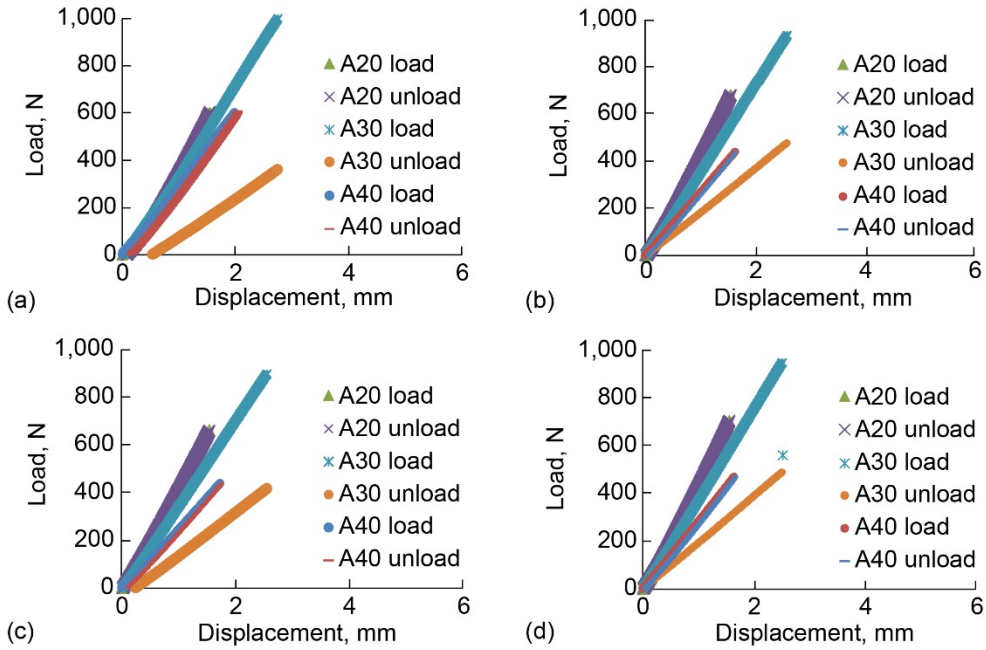

Figure 3.—Compliance calibration and non-precracked test results from specimen set 1 control (no shape memory alloy). (a) 1-1. (b) 1-2. (c) 1-3. (d) 1-4.

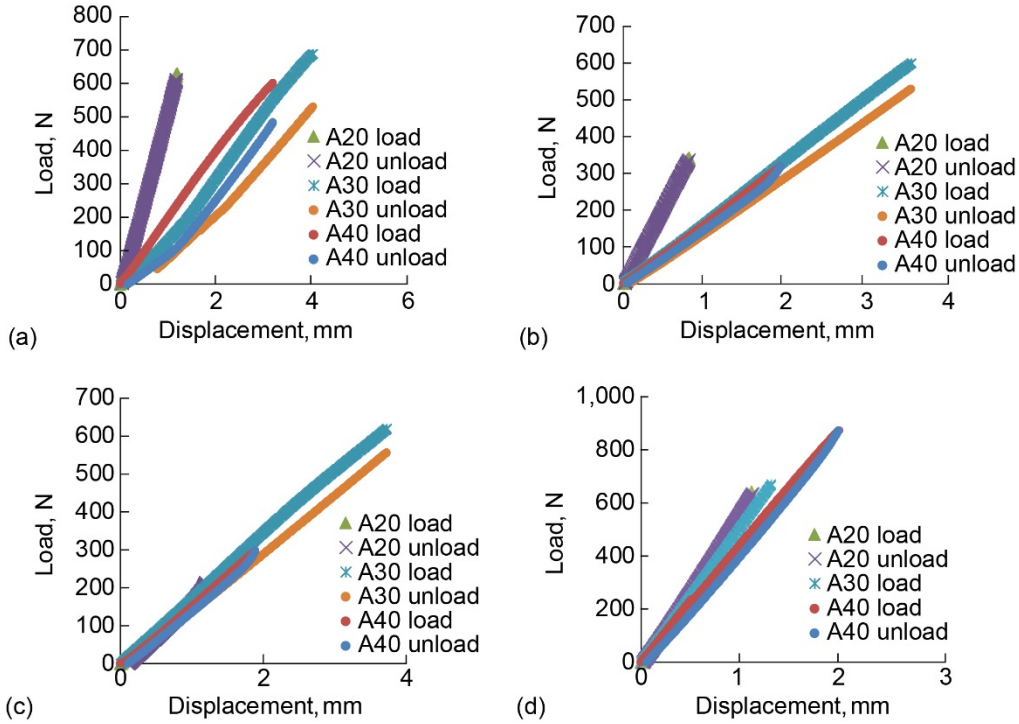

Figure 4.—Compliance calibration and non-precracked test results from specimen set 2 shape memory alloy (no adhesive). (a) 2-1. (b) 2-2. (c) 2-3. (d) 2-4.

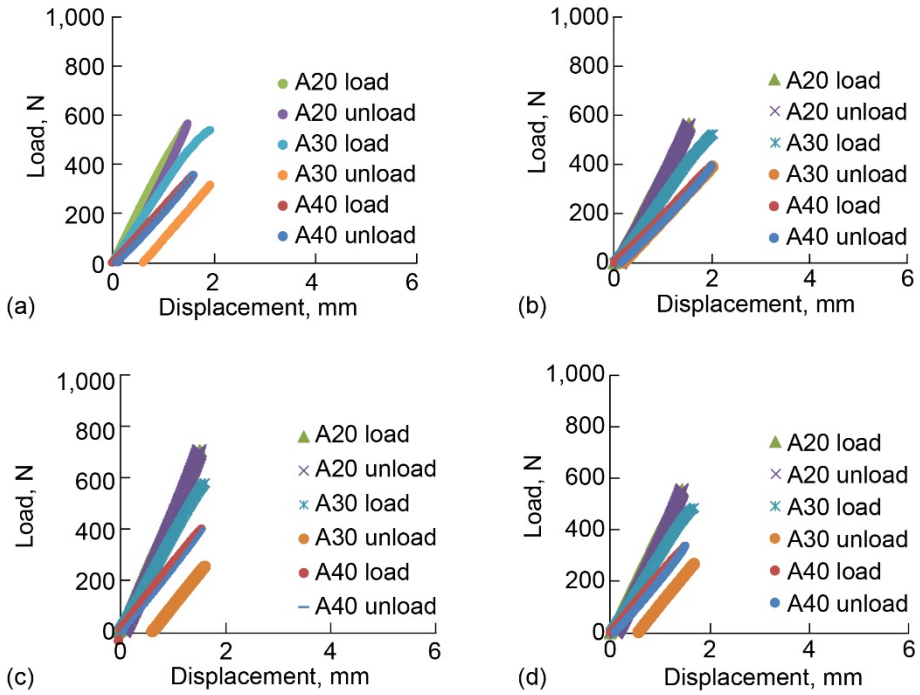

Figure 5.—Compliance calibration and non-precracked test results from specimen set 3 shape memory alloy (FM® 377U adhesive). (a) 3-1. (b) 3-2. (c) 3-3. (d) 3-4.

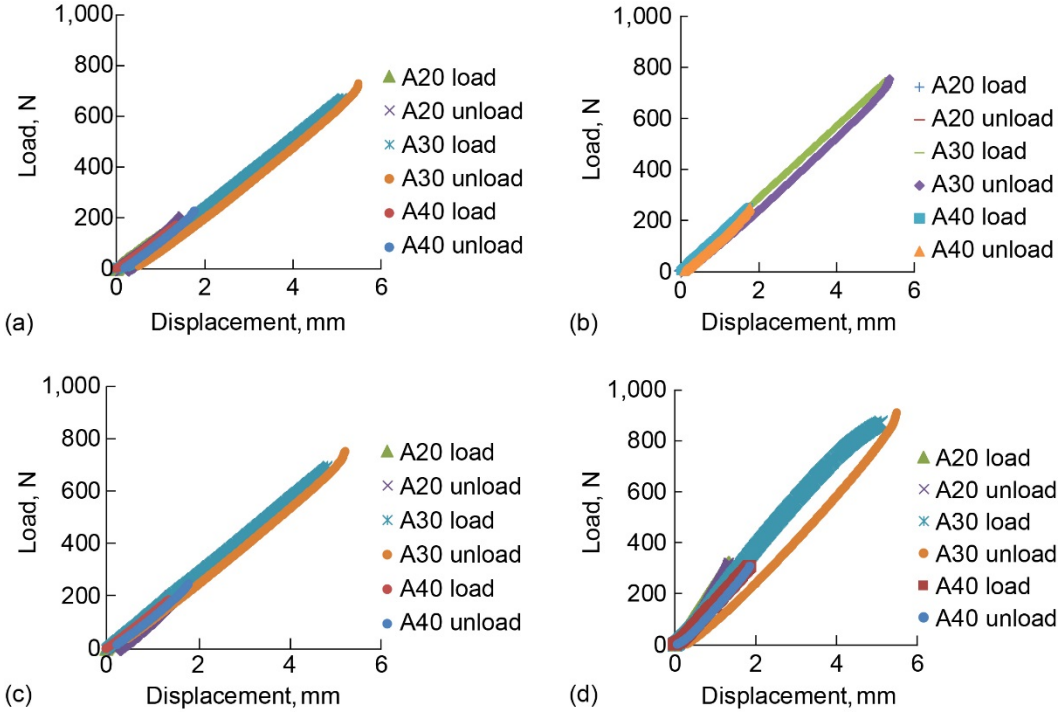

Figure 6.—Compliance calibration and non-precracked test results from specimen set 4 shape memory alloy (Hysol® EA9696 adhesive). (a) 4-1. (b) 4-2. (c) 4-3. (d) 4-4.

The four different graphs for each figure indicate the individual specimens that made up each test group (four specimens for control, four specimens for the SMA group, etc.). The graphs in Figure 3 show distinctly different slopes of the three different compliances used, which is typical of a composite system. The addition of the SMA (with and without a system) shows a difference in that the slopes of the different compliances are all very close in relation to each other. This shows the effect that the inner SMA ply has on the total flex of the system. Overall, Figure 3 to Figure 6 shows that the flex of the system is not only increased by the addition of the SMA, but is normalized no matter where the compliance of the system is loaded at (A20, A30, or A40).

3.2 Acoustic Emission (AE) Results

Acoustic signals generated during double cantilever beam (DCB) testing were recorded by the WaveExplorer software via the acoustic sensors and preamplifier. Cumulative AE is plotted alongside the load data for each of the test specimens to better correlate acoustic signals originating from the mechanical events. Acoustic events were only detected during the crack propagation phase; such data are presented in Figure 7 to Figure 10.

For the majority of graphs seen in Figure 7 to Figure 10, a minimal amount of acoustic energy is detected within the ENF system during testing. This indicates that the mechanism of failure in these specimens (despite propagating a crack) cannot necessarily be detected and tracked via AE.

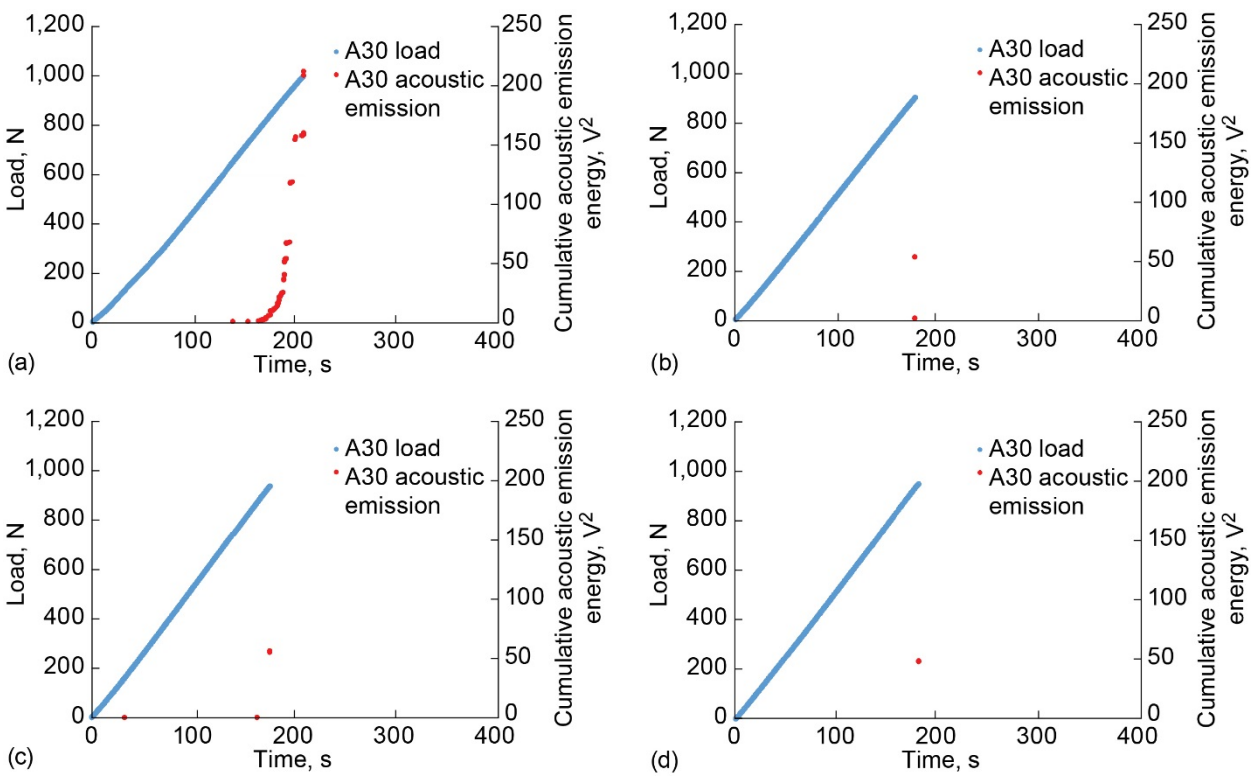

Figure 7.—Cumulative acoustic emission plotted alongside load for control series. (a) 1-1. (b) 1-2. (c) 1-3. (d) 1-4.

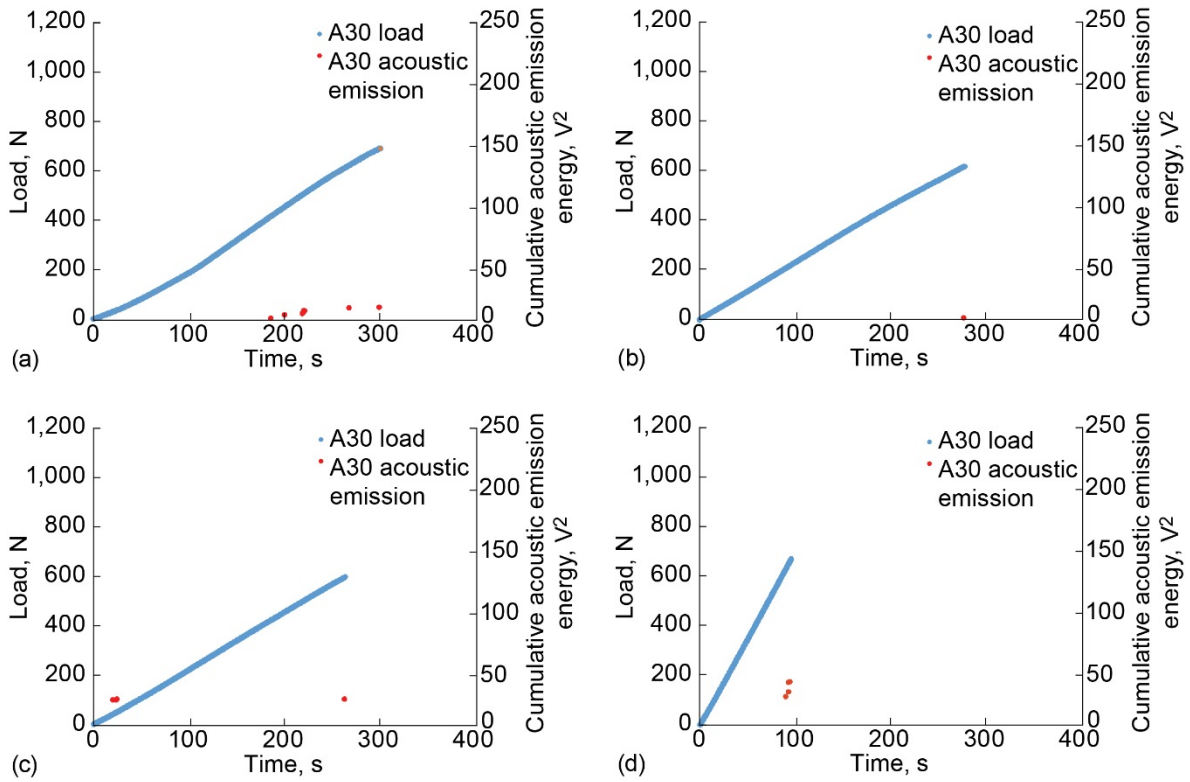

Figure 8.—Cumulative acoustic emission plotted alongside load for shape memory alloy control series. (a) 2-1. (b) 2-2. (c) 2-3. (d) 2-4.

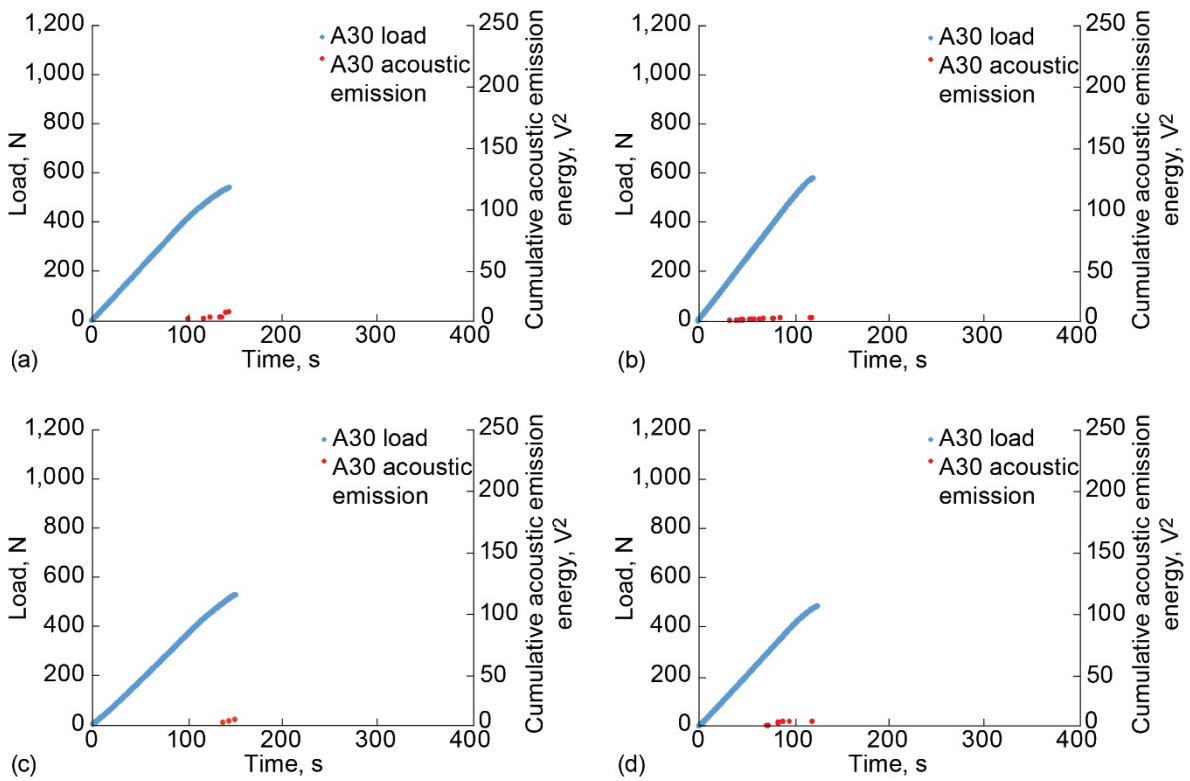

Figure 9.—Cumulative acoustic emission plotted alongside load for shape memory alloy and FM® 377U Series. (a) 3-1. (b) 3-2. (c) 3-3. (d) 3-4.

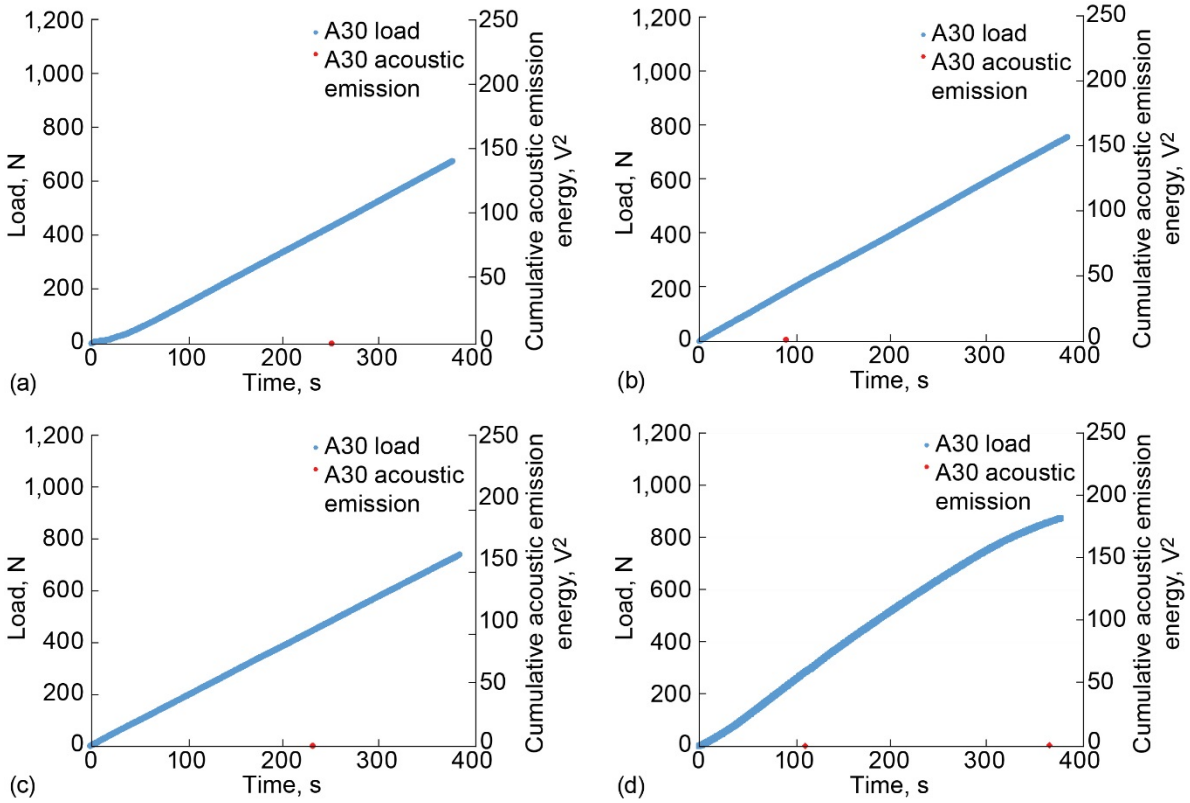

Figure 10.—Cumulative acoustic emission plotted alongside load for shape memory alloy and Hysol® EA9696 Series. (a) 4-1. (b) 4-2. (c) 4-3. (d) 4-4.

3.3 C-Scan and Microscopy Results

The effect of the SMA inserts and adhesives on the ENF test results was evaluated by examining the images taken using C-scan, optical microscopy, and SEM methods. The images of the sections of the specimen interiors before and after mechanical testing were compared. These images highlighted the effect of the insert, the nature of the adhesives used, and the issues that caused irregular results in ENF testing.

3.3.1 C-Scan Results

The quality of specimen panels was examined by C-scan. The results are shown in Figure 11. In these images, the dark orange or red colors from the C-scan are indicative of a well-consolidated part. The zones with dark or lighter blue color indicate poor bonding, while white sections typically represent the voids or unbonded areas. Figure 11(a) shows that the control specimen is a well-consolidated part, while the addition of SMA in Figure 11(b) is a poorly bonded part. The addition of adhesive in Figure 11(c) and (d) does not improve this bond according to the C-scan plots.

3.3.2 Photography

Before optical microscopy was performed, photographs were taken of the parts after testing. Specimens 1-1, 2-1, 3-2, and 4-2 were separated along the debonding line after testing and photographs were taken. These images are shown in Figure 12 to Figure 15.

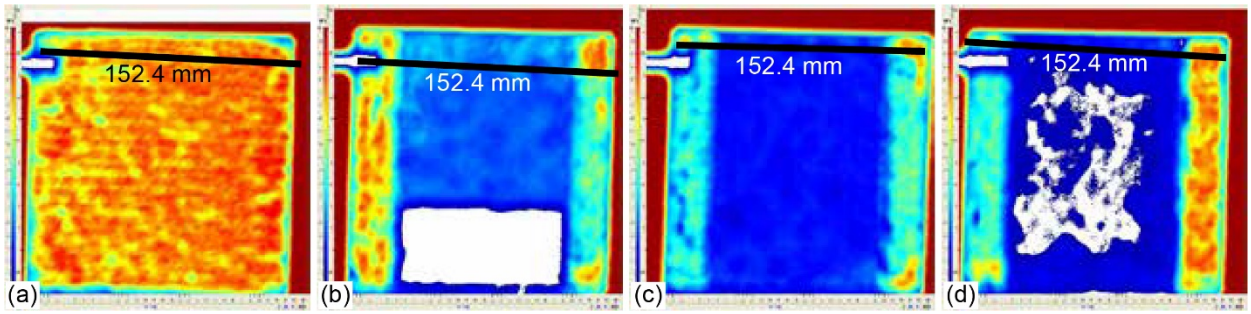

Figure 11.—C-scans of end-notched flexure panels before testing. (a) Control panel. (b) Shape memory alloy (SMA) control panel. (c) SMA and FM® 377U panel. (d) SMA and Hysol® EA9696 panel.

Figure 12.—Specimen 1-1. (a) Top half. (c) Bottom half.

Figure 13.—Specimen 2-1. (a) Top half polymer matrix composite. (b) Bottom half shape memory alloy.

3.3.3 Optical Microscopy

The optical microscope images taken were for the same specimens shown above: 1-1, 2-1, 3-2, and 4-2. Figure 16 to Figure 19 show images of two sections of these specimens, the insert end and the crack end.

Figure 14.—Specimen 3-2. (a) Top half polymer matrix composite. (b) Bottom half shape memory alloy.

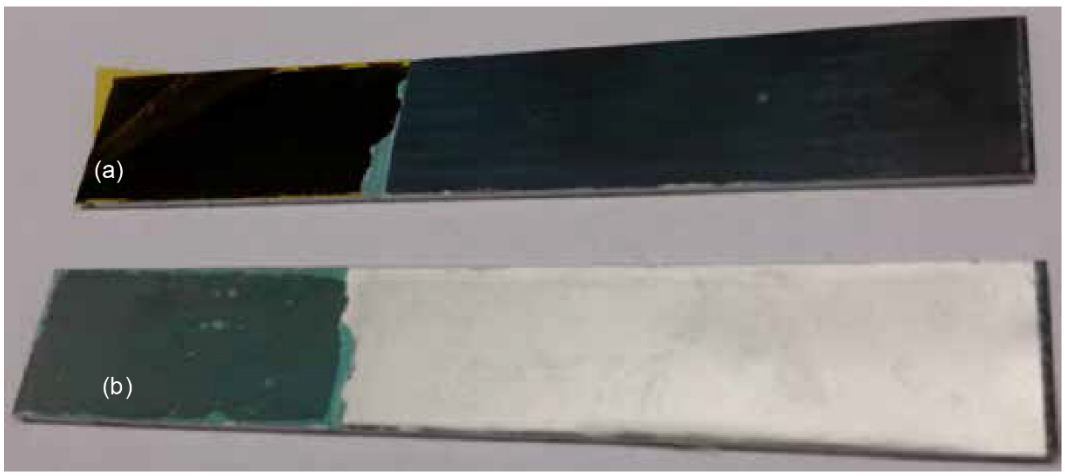

Figure 15.—Specimen 4-2. (a) Top half polymer matrix composite. (b) Bottom half shape memory alloy.

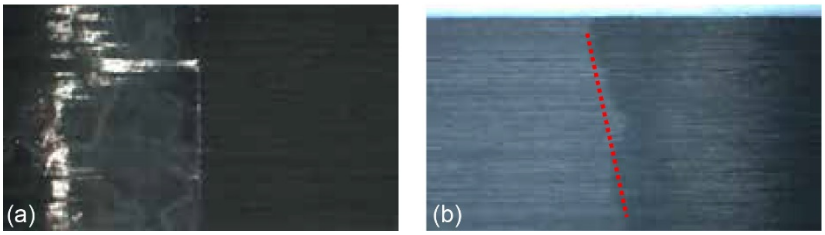

Figure 16.—Optical microscopy of specimen 1-1. (a) Crack insert end. (b) Crack end.

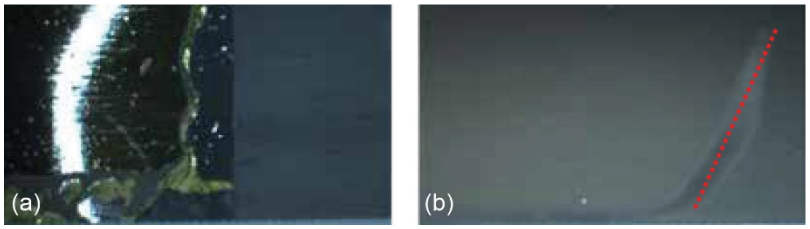

Figure 17.—Optical microscopy of specimen 2-1. (a) Crack insert end. (b) Crack end.

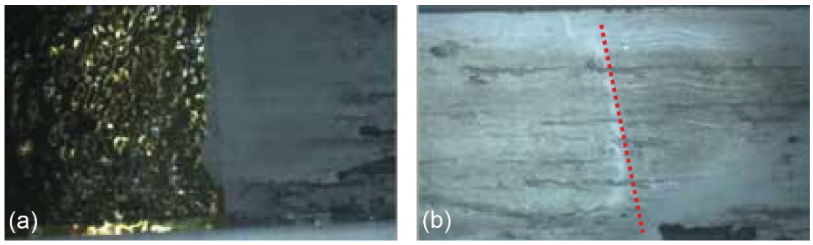

Figure 18.—Optical microscopy of specimen 3-2. (a) Crack insert end. (b) Crack end.

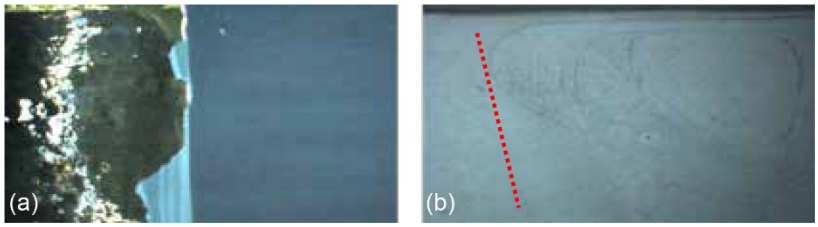

Figure 19.—Optical microscopy of specimen 4-2. (a) Crack insert end. (b) Crack end.

3.3.4 Scanning Electron Microscopy (SEM)

SEM images were taken of the area in which the precrack insert was placed, along with the area in which crack propagation occurred. Figure 20 shows the precrack and crack propagation area of specimen 1-1.

There is a noticeable difference in the debond area where the insert was compared to where actual crack propagation progressed through the control specimen. This includes not only a rougher surface, but broken fibers and matrix areas as well. Figure 21 shows similar images for specimen 2-2, the specimen with SMA and no added adhesive.

In these images, the surface roughness between precrack and crack sections is readily recognized by the transition from smooth crack to rough. Comparing this image to that in Figure 20, the crack propagation section for the SMA control sample conformed to the shape of the SMA material and did not progress through any plies of the PMC itself; this is the reason why the surface is smoother and without any noticeable fiber breaks. The distinct pattern seen in Figure 21(b) is actually that of the PMC when conformed against the SMA material.

Figure 22 shows the precrack and crack propagation section of specimen 3-2, the ENF specimen that utilized the FM® 377U adhesive between PMC and SMA.

Similar to Figure 21, the images in Figure 22 show the difference in surface roughness between the precrack area of the specimen (where the insert was) when compared to the crack section of the specimen. Unlike the control specimen, however, this specimen shows signs of adhesive in Figure 22(b). While an imprint of the SMA material is seen, sections of Figure 22(b) show various cracks and delaminations between the SMA imprint and adhesive. This shows that the majority of FM® 377U adhesive remained alongside the PMC during ENF testing, while actively debonding from the SMA during the test.

Figure 23 shows the precrack and crack propagation section of specimen 4-1, the ENF specimen that utilized Hysol® EA9696 adhesive between PMC and SMA.

Again, note the difference in surface roughness between the precrack area of the specimen (where the insert was) against the crack section of the specimen. Unlike Figure 22, however, the specimen with Hysol® EA9696 as the adhesive shows an even higher extent of bonding with the PMC layer. This is seen in Figure 23(b), where little to no ridges or delaminations are seen in the images taken. This indicates that little to no material stayed adhered to the SMA during the ENF testing.

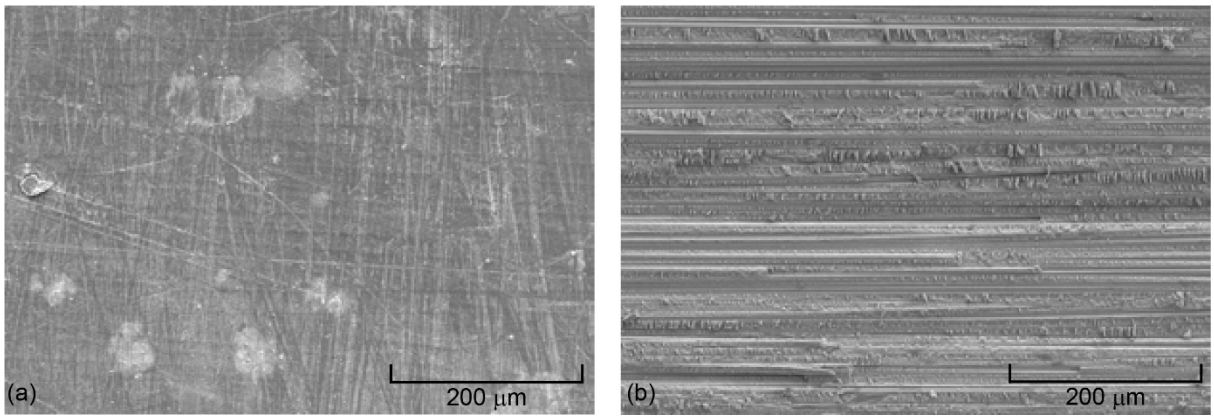

Figure 20.—Scanning electron microscopy of control series specimen 1-1. (a) Precrack propagation section. (b) Crack propagation section.

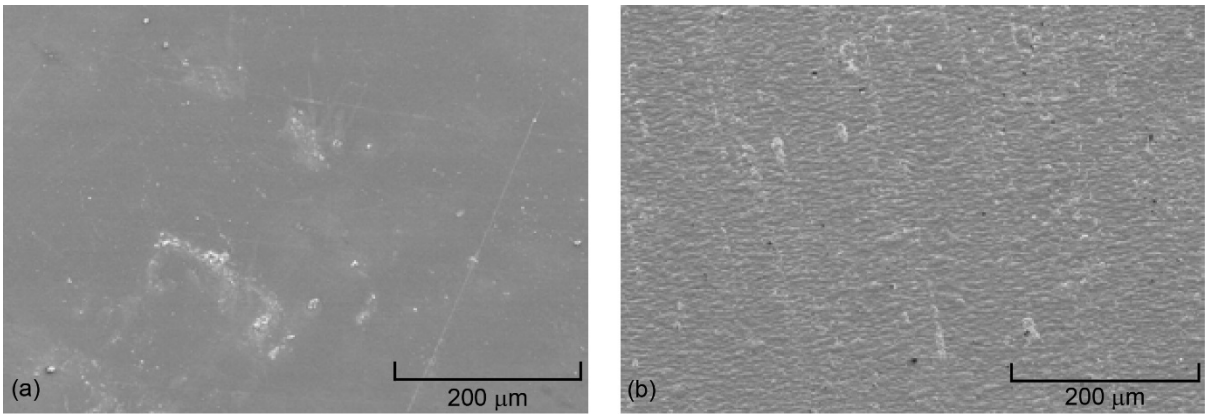

Figure 21.—Scanning electron microscopy of shape memory alloy control series specimen 2-2. (a) Precrack propagation section. (b) Crack propagation section.

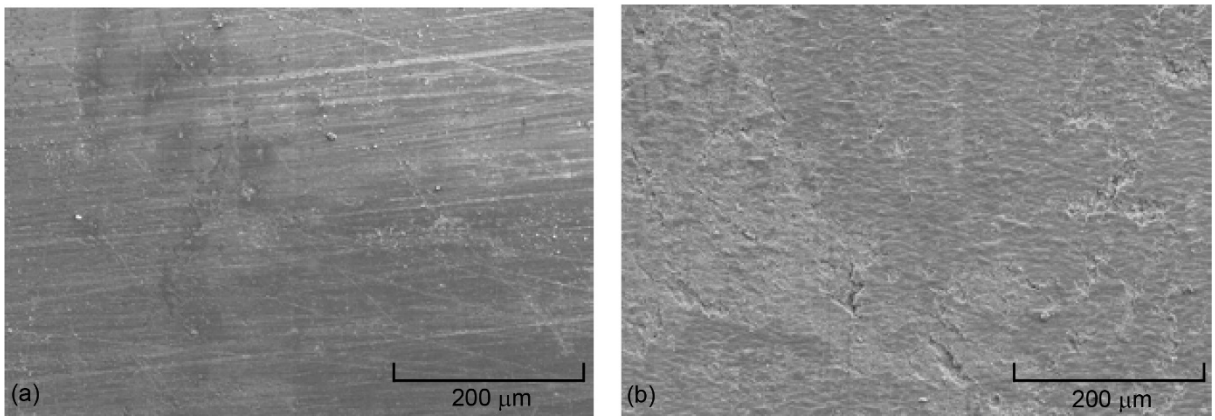

Figure 22.—Scanning electron microscopy of shape memory alloy and FM® 377U series specimen 3-2. (a) Precrack propagation section. (b) Crack propagation section.

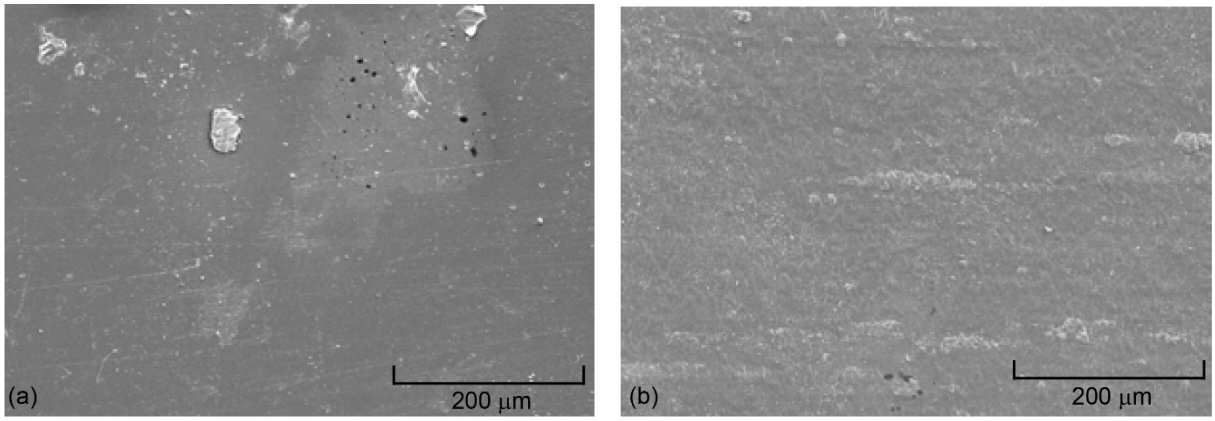

Figure 23.—Scanning electron microscopy of shape memory alloy and Hysol® EA9696 series specimen 4-1. (a) Precrack propagation section. (b) Crack propagation section.

4.0 Analysis

The results from ENF testing were analyzed in order to highlight the differences in interlaminar strengths between the sets of specimens. This analysis includes a compliance calibration overview of the samples, which then leads to mode II interlaminar fracture toughness, G_{IIC}, values for each of the specimens.

4.1 Compliance Calibration

The compliance calibration (CC) method was performed on the non-precracked (NPC) fracture tests. This method involves loading the specimens at different crack lengths in order to obtain a value of compliance from each test. Figure 24 shows a typical ENF load-displacement plot from NPC fracture test specimen 1-3.

For each crack length, a value of compliance was determined by a least-squares linear regression analysis of the data to obtain the slope of the displacement versus load data. The compliances found were plotted against the corresponding tested compliance length distances (A20, A30, A40) raised to the third power and fit to a line via Equation (1).

$$C = A + ma^3 \tag{1}$$

In Equation (1), a is the delamination length, A is the intercept of linear fit of compliance versus crack length cubed data, C is the specimen compliance, and m is the compliance calibration coefficient.

Figure 25 shows a fit of Equation (1) with the experimental data, where compliance is plotted against the crack value for each plot in Figure 24.

The resulting values from Equation (1) were used to find the value of mode II interlaminar fracture toughness, G_{IIC}. This toughness value is determined using Equation (2).

$$G_{IIC} = \frac{3mP_{\max}^2 a_o^2}{2B} \tag{2}$$

In Equation (2), G_{IIC} is the mode II interlaminar fracture toughness, $P_{\max}$ is the maximum force from fracture testing, a_o is the crack length used for the fracture test (30 mm), and B is the specimen width.

The average G_{IIC} values from each specimen series were summarized for comparative analysis in Figure 26.

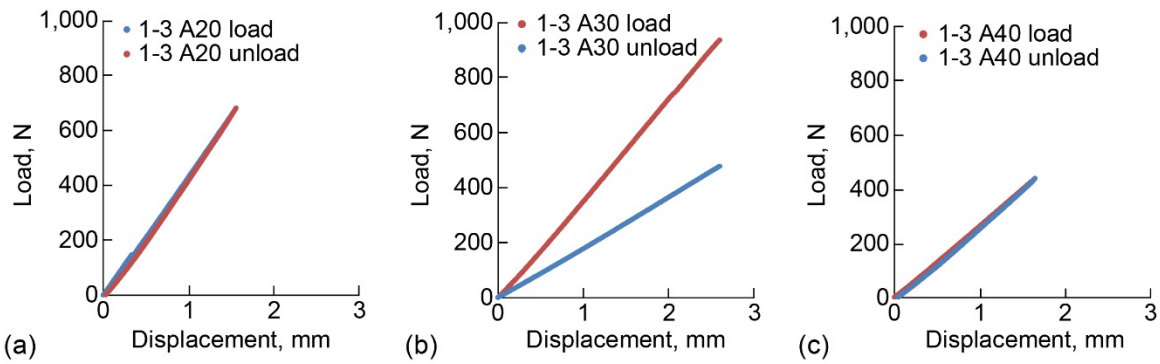

Figure 24.—Compliance calibration load displacement plots for specimen 1-3. (a) a_o = 20 mm. (b) a_o = 30 mm. (c) a_o = 40 mm.

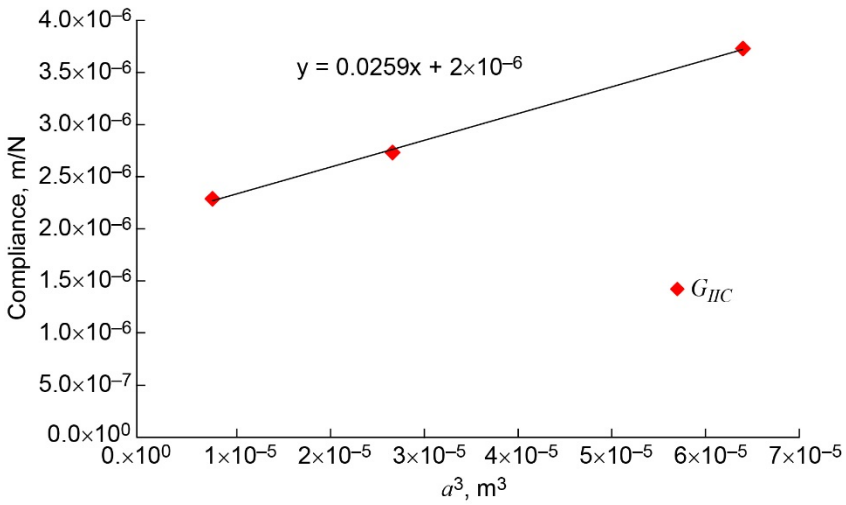

Figure 25.—Compliance versus crack length plots for specimen 1-3, where $a = 2\times10^{-6}$ and m = 0.026.

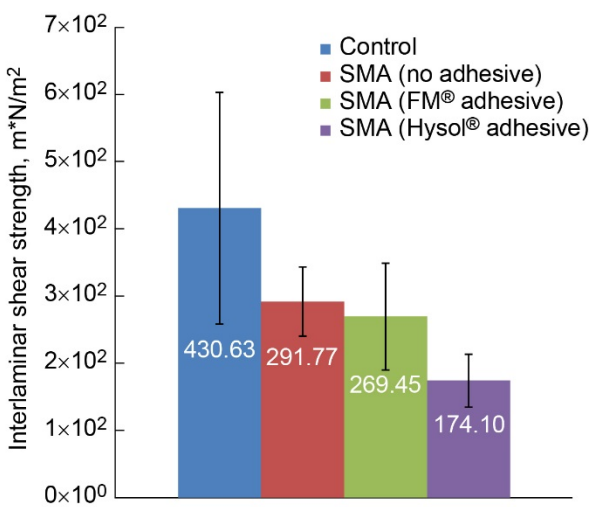

Figure 26.—Fracture toughness averages for end-notched flexure testing. SMA, shape memory alloy.

Variation in calculated G_{IIC} values resulted in large standard deviations for the control series. Standard deviations were lower for specimens with embedded SMAs. This is attributed to variation within specimens during fabrication and testing.

5.0 Discussion

Calculated G_{IIC} results from this study were significantly lower than G_{IIC} values found in literature (Refs. 18 and 22). G_{IIC} values from this study averaged 2.46 in•lbf/in². ASTM interlaboratory studies (Ref. 18) G_{IIC} values were 5.18 in•lbf/in², while independent research by O'Brien (Ref. 22) found G_{IIC} values of 6.5 in•lbf/in². Analysis of difficulties during our study can reveal why results found were lower than those found by previous researchers.

5.1 End-Notched Flexure (ENF) Background

The ENF method was developed in the late 1970s by Barrett and Foschi (Ref. 23). This was later adapted by Russell and Street (Ref. 24), who developed the earliest analytical expressions for mode II strain energy release rate (G_{II}) and specimen compliance. Subsequently, derivation of expressions of G_{IIC} for a variety of test methods was proposed. These include three-point bending (Ref. 23), four-point bending (Ref. 25), end-loaded split (Ref. 26), and tapered ENF methods (Ref. 27). The departure from the three-point bending test was driven by the following rationale: the crack propagation seen in three-point bending tests for obtaining G_{IIC} values is unstable, leading to generation of only one data point per test, as opposed to the multiple G_{IC} values generated from a single DCB test. A number of research papers (Refs. 28 to 38) have all stated this issue and looked to correct or better estimate fracture toughness values from three-point bending ENF tests.

Aside from irregular crack growth propagation, other issues in ENF testing have also been found including specimen thickness and curing pressure (Ref. 37), bending rotations (Ref. 35), nonlinear interface fracture (Ref. 32), process zone phenomenon (Ref. 30), and even the friction between the loading pin and the ENF specimen (Ref. 33). Any one of these variables, along with those generated from the insertion of an SMA into the specimen, can be the cause of such low G_{IIC} values within tested specimens. There were specific examples of issues that arose during testing that may be attributed to these low values.

5.2 Issues in End-Notched Flexure (ENF) Testing

Specimen fabrication itself leads to a handful of issues that may be the underlying cause for the low G_{IIC} values gathered from test results. Initial fabrications of the panels included a 12.7-µm polyimide insert. No noticeable crack propagation was observed during testing. A bonding between the insert and the epoxy matrix of the HexPly® 8552/IM7 material was revealed upon opening of the specimens after testing. To alleviate the issues due to epoxy-insert bonding, a final set of specimens were fabricated that included a baked-on coating of a release agent, Frekote® (Henkel Corporation), onto the precrack insert. The addition of this release agent onto the insert allowed for successful testing, as seen in Figure 27. There is a distinct possibility, however, that the release agent may have propagated through the PMC and along the bond line of the specimen. Other researchers also observed such a phenomenon (Ref. 30).

An issue within the Bluehill® software was also observed before actual testing. According to the ENF ASTM standard (Ref. 18), the three-point bend test should be run at a set rate (between 0.1 and 0.8 mm/min) until reaching a preset loading, based upon initial compliance calibration calculations. This was not

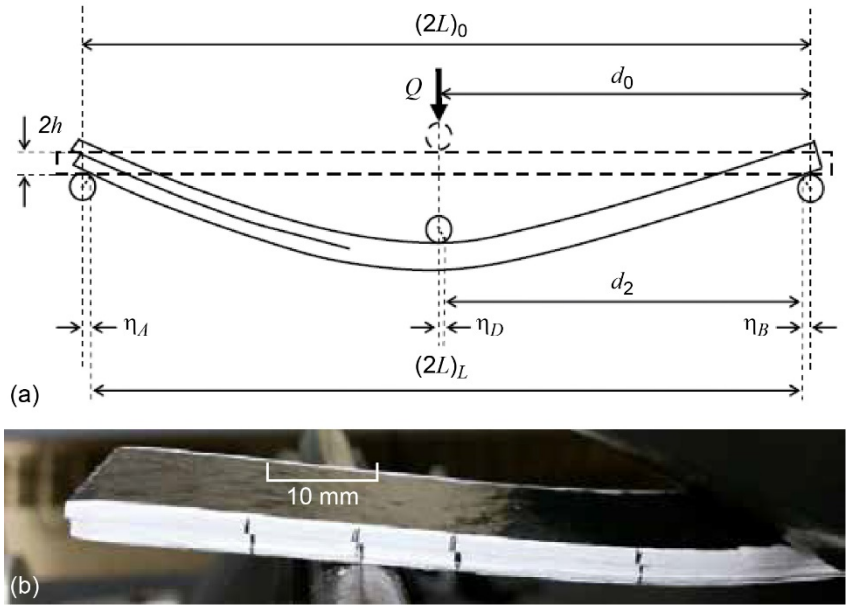

Figure 27.—(a) Theoretical crack propagation of end-notched flexure specimen. (b) Actual crack propagation of tested specimen. Where d_0 is distance from center of support roller at uncracked end of specimen to uncracked end of specimen (theoretical), d_2 is distance between bend radii of loading and support roller at uncracked end (theoretical), h is specimen thickness, h_A is difference between center of support roller and bend radius at cracked end (theoretical), h_B is distance between center of support roller and radius bend point at uncracked end (theoretical), and h_D is difference between center loading roller and radius bend point (theoretical), and Q is downward force on loading roller.

achievable with the Bluehill® software; the system could only be run according to either load rate or load force. This meant that mixing the two, as required by the standard, could not be achieved. To circumvent this issue, extra specimens were included in tests; the loads for failure and compressive distances were recorded. From this information, set compressive distances were used for compliance calibration at the varying crack insert values. While this did achieve the intended result for compliance calibration, straying from the ASTM standard may have had unintended consequences for G_{IIC} calculations.

5.3 Mode II Interlaminar Fracture Toughness (G_{IIC}) Values

Despite the issues that may have arisen from fabrication or testing, or from issues within the use of the ENF standard itself, the fact remains that the tested specimens were all subjected to identical conditions as far as fabrication and testing are concerned. While the comparison between control specimen G_{IIC} values and other reported G_{IIC} values may have discrepancies, the G_{IIC} values observed from testing are still comparable.

To understand the variation between G_{IIC} values of specimens, the C-scans of the panels must be looked at. In Figure 11, it can be inferred that the control panel had the best overall bonding among all test specimens. A qualitative comparison of the remaining C-scans shows that the bond became poorer from Figure 11(a) to (d); the control sample with SMA was noticeably worse than the control sample, but bonding was not improved with the addition of the adhesive.

Comparing the C-scan images with the photographs and optical microscopy images further shows issues with bonding. Figure 13 and Figure 14 show considerable amounts of adhesive (either epoxy or FM® 377U), while Figure 15 shows the lack of Hysol® EA9696 adhesive bonded to the SMA. These images are further magnified in Figure 17 and Figure 18; and while there are definite signs of epoxy and FM® 377U adhesive on the SMA surface, there is only a trace residue of Hysol® EA9696 on the SMA surface of that particular specimen. Another major issue that caused poor G_{IIC} values was the pooling of epoxy material, either on the SMA itself (Figure 17) or within the additional adhesive. This phenomenon is stated as a cause for poor bonding and G_{IIC} values within the ENF standard and can account for the lowered interfacial toughness of these specimens.

Analysis of the SEM images showed that even with the addition of adhesives, the majority of the added adhesive sheared away cleanly from the SMA surface, adhering only to the PMC. Figure 22 and Figure 23 reflect this, showing some delamination of the adhesive layer within the FM® 377U specimen versus no delamination of the Hysol® EA9696 specimen. This adhesive preference is further reflected in the G_{IIC} results, where the FM® 377U adhesive material performed better than the Hysol® EA9696 material, though both gave poorer results than the SMA control specimen.

As a final reflection of the instability of the bond within the test specimens, AE signals for the majority of the tests were nonexistent. Only in the first test of the control series was a significant amount of AE seen. The rest of the specimens generated a minimal amount of AE during testing. The images from C-scans, optical microscopy, and SEM further can be coupled along with the lack of AE data to highlight the poor quality of the bond within the tested specimens, despite the use of adhesives to improve the bond.

6.0 Conclusion

The bond between ply layers in a carbon fiber reinforced polymer (CFRP) composite is a focal point for failure in a variety of modes. Exploration of this failure mode for in-plane shear (mode II) produces a wide deviation of results. Despite the recent adoption of three-point bend testing for end-notched flexure (ENF) as an ASTM standard, the test itself has a history of varied results within set materials due to the unstable growth of the interlaminar crack during testing. The addition of shape memory alloy (SMA) material between plies exacerbates this failure mode. The use of adhesives without any additional preparation of the SMA surfaces lowered interlaminar properties within the composite. The poor bonding was reflected not only in the C-scans before testing, but in the results of optical and scanning electron microscopy (SEM) microscope images of test specimens after failure. The lack of acoustic signals generated during testing was also an indicator that bonding was insufficient between the SMA and polymer matrix composite (PMC) for in-plane shear. An increase in the bond between the adhesive layers and SMA must be optimized via chemical or physical means before any significant gains in interlaminar fracture toughness can be achieved within a CFRP.

Appendix—Nomenclature

AE	acoustic emission
CC	compliance calibration
CFRP	carbon fiber reinforced polymer
DCB	double cantilever beam
ENF	end-notched flexure
NPC	non-precracked
PMC	polymer matrix composite
SEM	scanning electron microscopy
SMA	shape memory alloy

Symbols

a	delamination length
a_i	distance
a_o	crack length
A	intercept of linear fit of compliance versus crack length cubed data
B	specimen width
C	specimen compliance
d_0	distance from center of support roller at uncracked end of specimen to uncracked end of specimen (theoretical)
d_2	distance between bend radii of loading and support roller at uncracked end (theoretical)
G_{IC}	mode I interlaminar toughness
G_{II}	mode II strain energy release rate
G_{IIC}	mode II interlaminar fracture toughness
h	specimen thickness
L	specimen half span
L_C	distance from center of support roller at cracked end of specimen to cracked end of specimen
L_U	distance from center of support roller at uncracked end of specimen to uncracked end of specimen
m	compliance calibration coefficient
$P_{\max}$	maximum force from fracture testing
Q	downward force on loading roller
r_1	radius of loading roller
r_2	radius of support roller
x	distance between the two sensors
Δt_x	difference in arrival time
h_A	difference between center of support roller and bend radius at cracked end (theoretical)
h_B	distance between center of support roller and radius bend point at uncracked end (theoretical)
h_D	difference between center loading roller and radius bend point (theoretical)

References

1. de Araujo, C.J., et al.: Fabrication and Static Characterization of Carbon-Fiber-Reinforced Polymers With Embedded NiTi Shape Memory Wire Actuators. Smart Mater. Struct., vol. 17, no. 6, 2008.
2. Bollas, D., et al.: Stress Generation by Shape Memory Alloy Wires Embedded in Polymer Composites. Acta Mater., vol. 55, no. 16, 2007, pp. 5489–5499.
3. Parthenios, J.; Psarras, G.C.; and Galiotis, C.: Adaptive Composites Incorporating Shape Memory Alloy Wires. Part 2: Development of Internal Recovery Stresses as a Function of Activation Temperature. Composites: Part A, vol. 32, 2001, pp. 1735–1747.
4. Schrooten, Jan, et al.: Progress on Composites With Embedded Shape Memory Alloy Wires. Mater. Trans., vol. 43, no. 5, 2002, pp. 961–973.
5. Turner, Travis L.; Lach, Cynthia L.; and Cano, Roberto J.: Fabrication and Characterization of SMA Hybrid Composites. Proceedings of the SPIE Smart Structures and Materials 2001, Vol. 4333, 2001, pp. 33–43.
6. Hisaaki, Tobushi, et al.: Thermomechanical Properties of Shape-Memory Alloy and Polymer and Their Composites. Mech. Adv. Mater. Struc., vol. 16, 2009, pp. 236–247.
7. Turner, Travis L., et al.: Modeling, Fabrication, and Testing of a SMA Hybrid Composite Jet Engine Chevron Concept. J. Intell. Material Syst. Struct., vol. 17, no. 6, 2006, pp. 483–497.
8. Kim, Cheol; Park, Bum-Sik; and Goo, Nam-Seo: Shape Changes by Coupled Bending and Twisting of Shape-Memory-Alloy-Embedded Composite Beams. Smart Mater. Struct., vol. 11, 2002, pp. 519–526.
9. Ostachowicz, W.; Krawczuk, M.; and Zak, A.: Dynamics and Buckling of a Multilayer Composite Plate With Embedded SMA Wires. Compos. Struct., vol. 48, nos. 1–3, 2000, pp. 163–167.
10. Poon, Chi-kin, et al.: Interfacial Debond of Shape Memory Alloy Composites. Smart Mater. Struct., vol. 14, no. 4, 2005, pp. 29–37.
11. Song, Gangbing, et al.: Application of Shape Memory Alloy Wire Actuator for Precision Position Control of a Composite Beam. J. Mater. Eng. Perform., vol. 9, no. 3, 2000, pp. 330–333.
12. Shu, Steven G., et al.: Modeling of a Flexible Beam Actuated By Shape Memory Alloy Wires. Smart Mater. Struct., vol. 6, no. 3, 1997, pp. 265–277.
13. Hebda, Derek A.; and White, Scott R.: Structural Behavior of SMA Composite Beams. American Society of Mechanical Engineers, Applied Mechanics Division, vol. 206, 1995, pp. 111–119. https://iwe.pure.elsevier.com/en/publications/structural-behavior-of-sma-composite-beams Accessed June 14, 2018.
14. Duering, T.W., et al.: Engineering Aspects of Shape Memory Alloys. Butterworth-Heinemann, London, 1990.
15. Paine, J.S.N.; and Rogers, C.A.: Review of Multi-functional SMA Hybrid Composites Materials and Their Applications. Adaptive Structures and Composite Materials: Analysis and Application vol. 54, 1994, pp. 37–45.
16. Xu, Ya, et al.: A New Method for Fabricating SMA/CFRP Smart Hybrid Composites. Intermetallics, vol. 10, 2002, pp. 361–369.
17. Jang, Byung-Koog; and Kishi, Teruo: Thermomechanical Response of TiNi Fiber-Impregnated CFRP Composites. Mater. Lett., vol. 59, nos. 19–20, 2005, pp. 2472–2475.
18. ASTM D7905: Standard Test Method for Mode II Interlaminar Fracture Toughness of Unidirectional Fiber-Reinforced Polymer Matrix Composites. ASTM International, Conshohocken, PA, 2014.
19. Hexcel Composites: Hexply 8552 Material Safety Data Sheet. April 1, 2009. https://shedapps.grc.nasa.gov/pdf/MSDS2010/grc-5038a-462.pdf Accessed June 15, 2018.
20. Henkel Corporation: Loctite EA 9696 15UNS AERO Safety Data Sheet, IDH No. 698917, Aug. 13, 2015. http://hybris.cms.henkel.com/henkel/msdspdf?matnr=698917&country=US&language=EN Accessed June 15, 2018.

21. Cytec Engineered Materials: FM 377U Adhesive Film. Technical Data Sheet ID No. AEAD–00014, April 7, 2010. http://www.cytec.com/sites/default/files/datasheets/FM_377_040710.pdf Accessed May 2015.
22. O'Brien, T. Kevin; Johnston, William M.; and Toland, Gregory J.: Mode II Interlaminar Fracture Toughness and Fatigure Characterization of a Graphite Epoxy Composite Material. NASA/TM—2010-216838, 2010. http://ntrs.nasa.gov
23. Barrett, J.D.; and Foschi, R.O.: Mode II Stress-Intensity Factors for Cracked Wood Beams. Eng. Fract. Mech., vol. 9, no. 2, 1977, pp. 371–378.
24. Russell, A.J.; and Street, K.N.: Factors Affecting the Interlaminar Fracture Energy of Graphite/Epoxy Laminates. Reprinted from Progress in Science and Engineering of Composites, Paper published in Proceedings of the 4th International Conference on Composite Materials, REPR–83–12, Tokyo, 1982, pp. 279–286.
25. Martin, R.H.; and Davidson, B.D.: Mode II Fracture Toughness Evaluation Using Four Point Bend, End Notched Flexure Test. Plast. Rubber Compos., vol. 28, no. 8, 1999, pp. 401– 406.
26. Wang, H.; and Vu-Khanh, T.: Use of End-Loaded-Split (ELS) Test To Study Stable Fracture Behaviour of Composites Under Mode II Loading. Compos. Struct., vol. 36, nos. 1–2, 1996, pp. 71–79.
27. Blackman, B.R.K.; Kinloch, A.J.; and Paraschi, M: The Determination of the Mode II Adhesive Fracture Resistance, G_{IIC}, of Structural Adhesive Joints: An Effective Crack Length Approach. Eng. Fract. Mech., vol. 72, no. 6, 2005, pp. 877–897.
28. Wang, Jialai; and Qiao, Pizhong: Novel Beam Analysis of End Notched Flexure Specimen for Mode-II Fracture. Eng. Fract. Mech., vol. 71, no. 2, 2004, pp. 219–231.
29. Martin, Roderick H.: Interlaminar Fracture Characterization: A Current Review. NASA Contractor Report 187573, 1991. http://ntrs.nasa.gov
30. Jumel, J., et al.: Instrumented End Notched Flexure—Crack Propagation and Process Zone Monitoring. Part I: Modelling and Analysis. Int. J. Solids Struct., vol. 50, no. 2, 2013, pp. 297–309.
31. Budzik, M.K., et al.: Instrumented End Notched Flexure—Crack Propagation and Process Zone Monitoring Part II: Data Reduction and Experimental. Int. J. Solids Struct., vol. 50, no. 2, 2013, pp. 310–319.
32. Ouyang, Zhenyu; and Guoqiang, Li: Nonlinear Interface Shear Fracture of End Notched Flexure Specimens. Int. J. Solids Struct., vol. 46, no. 13, 2009, pp. 2659–2668.
33. Renart, J., et al.: An Automated Methodology for Mode II Delamination Tests Under Fatigue Loading Based on the Real Time Monitoring of the Specimen's Compliance. Int. J. Fatigue, vol. 82, no. 3, 2016, pp. 634–642.
34. Prasad, B.K. Raghu; and Kumar, D.V.T.G. Pavan: Analysis of Composite ENF Specimen Using Higher Order Beam Theories. Thin Wall. Struct., vol. 46, no. 6, 2008, pp. 676–688.
35. Arrese, A.; and Mujika, F.: Influence of Bending Rotations on Three and Four-Point Bend End Notched Flexure Tests. Eng. Fract. Mech., vol. 75, no. 14, 2008, pp. 4234–4246.
36. Boyano, A., et al.: Experimental Assessment of an End Notched Flexure Test Configuration With an Inserted Roller for Analyzing Mixed-Mode I/II Fracture Toughness. Eng. Fract. Mech., vol. 163, 2016, pp. 462–475.
37. Sajith, S.; Arumugam, V.; and Dhakal, H.N.: Effects of Curing Pressure on Mode II Fracture Toughness of Unidirectional GFRP Laminates. Polym. Test., vol. 48, 2015, pp. 59–68.
38. Jagannathan, N.; Chandra, A.R. Anil; and Manjunatha, C.M.: Onset-of-Growth Behavior of Mode II Delamination in a Carbon Fiber Composite Under Spectrum Fatigue Loads. Compos. Struct., vol. 132, 2015, pp. 477–483.